Prestack inversion for porosity, shale volume, and sand probability in the Havert Formation of the Goliat field, southwest Barents Sea

Dzekamelive Honore Yenwongfai[1], Haque Nazmul Mondol[2], Inge Jan Faleide[3], Isabelle Lecomte[4], and Johan Leutscher[5]

Abstract

An integrated innovative multidisciplinary approach has been used to estimate effective porosity (PHIE), shale volume (V_{sh}), and sand probability from prestack angle gathers and petrophysical well logs within the Lower Triassic Havert Formation in the Goliat field, Southwest Barents Sea. A rock-physics feasibility study revealed the optimum petrofacies discriminating ability of extended elastic impedance (EEI) tuned for PHIE and V_{sh}. We then combined model-based prestack inversion outputs from a simultaneous inversion and an EEI inversion into a multilinear attribute regression analysis to estimate absolute V_{sh} and PHIE seismic attributes. The quality of the V_{sh} and PHIE prediction is shown to increase by integrating the EEI inversion in the workflow. Probability distribution functions and a priori petrofacies proportions extracted from the well data are then applied to the V_{sh} and PHIE volumes to obtain clean and shaly sand probabilities. A tectonic-controlled point-source depositional model for the Havert Formation sands is then inferred from the extracted sand bodies and the seismic geomorphological character of the different attributes.

Introduction

The past two decades have seen a significant increase in the use of quantitative seismic interpretation methods to characterize the subsurface. Quantitative seismic interpretation techniques are increasingly being implemented into reservoir characterization schemes to minimize hydrocarbon exploitation risks. The measured seismic data respond to the contrasts in the effective elastic properties in the subsurface area of investigation. However, the main goal is usually aimed at characterizing the different lithofacies, porosity distribution, and fluid content responsible for the effective elastic response. These underlying properties are only indirectly measured using the available proxies in the seismic data, which are then transformed to the geologic variables of interest using rock physics.

Direct hydrocarbon indicators (DHIs) from seismic data are not always successful because the seismic amplitude is a composite response of the saturated rock. Therefore, it is important to spend as much time characterizing the lithology response before fluid anomaly hunting. Reservoir quality assessment from seismic, well log, and laboratory data requires an integrated approach involving geology, petrophysics, rock physics, and geophysics. The shale volume (V_{sh}), cement volume, effective porosity (PHIE), and permeability are some important aspects of reservoir quality in siliciclastic reservoirs. Quantifying the probability of existence of a given facies of interest has consequences on the reservoir development plan (early field life) and can also be integrated in the enhanced oil recovery phase (late field life).

The Goliat field is located in the southeast of the Snøhvit field (Figure 1a) in the Norwegian sector of the Barents Sea in blocks 7122/7, 7122/8, and 7122/10. The field has been developed using the world's most advanced floating production, storage, and offloading (FPSO) unit with subsea templates. The Goliat field is the first oil field to be in production (March 2016) in the Norwegian Barents Shelf. The production will be supported by water and gas reinjection into the reservoir to maintain reservoir pressures. The main reservoir units are located within the Realgrunnen Subgroup and the Kobbe Formation. The Kobbe Formation is volumetrically the most important formation in the Goliat field in terms of the amount of estimated hydrocarbon reserves. Other minor reservoir units are the Klappmys and Snadd Formations.

[1]Statoil ASA, Oslo, Norway and University of Oslo, Oslo, Norway. E-mail: hyen@statoil.com; h.d.yenwongfai@geo.uio.no.
[2]University of Oslo, Oslo, Norway and Norwegian Geotechnical Institute (NGI), Oslo, Norway. E-mail: m.n.h.mondol@geo.uio.no; nhm@ngi.no.
[3]University of Oslo, Oslo, Norway. E-mail: j.i.faleide@geo.uio.no.
[4]University of Bergen, Bergen, Norway and University of Oslo, Oslo, Norway. E-mail: isabelle.lecomte@geo.uib.no; isabelle.lecomte@geo.uio.no.
[5]Eni Norge, Sandnes, Norway. E-mail: johan.leutscher@eni.com.

Manuscript received by the Editor 1 October 2016; revised manuscript received 17 March 2017; published ahead of production 15 May 2017. This paper appears in *Interpretation*, Vol. 5, No. 3 (August 2017); p. 1–19, 17 FIGS., 4 TABLES.
http://dx.doi.org/10.1190/INT-2016-0169.1.

This paper focuses on PHIE, V_{sh}, and sand distribution within the Lower Triassic Havert Formation using limited well-log data and good-quality multiazimuth (MAZ) seismic data. The base of the Havert Formation contains important sand units that have not been the focus in earlier studies in the Goliat area (Dario et al., 2013; Yenwongfai et al., 2016) because they are brine filled. A time structure map for the base Havert Formation with the relative locations of two available exploration wells are shown in Figure 1b. This is the first attempt of a seismic petrophysical evaluation of the Havert Formation in the study area. Despite being brine filled, a proper seismic lithology characterization in the Goliat area would be important for other Havert prospects in the wider Triassic Barents Shelf.

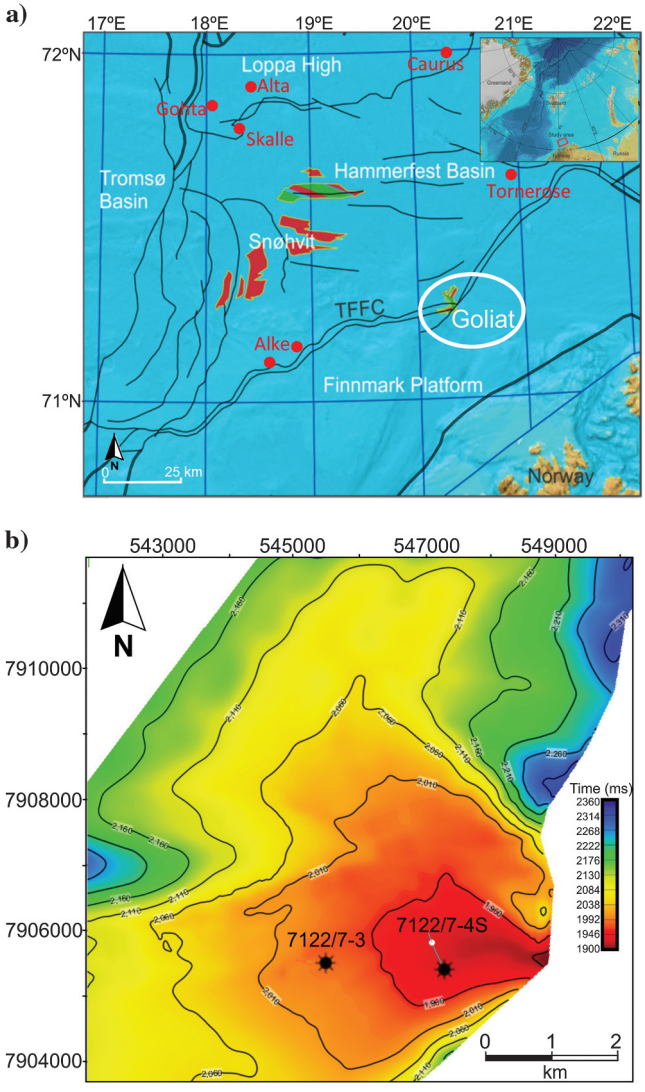

Figure 1. (a) Location of the Goliat field (adapted from NPD factmaps) in the Norwegian sector of the Barents Sea. The field is cut by the TFFC. The red dots show the position of other discoveries close to the Goliat field. (b) The time structure map for the base Havert Formation and the location of the two wells used in the study.

Geologic setting

The Uralian orogeny during Permian-Triassic times represents one of the latest collision elements in the study area prior to later extensional phases in the Late Paleozoic and Mesozoic times (Figure 2a). This led to the complex regional development of rift basins, structural highs, and platforms observed across the Barents Shelf (Johansen et al., 1993). The main regional structural elements in the Western Barents Sea are shown in Figure 2b. The focus of the main tectonic activity moved westward gradually with time. The most significant structural feature of a regional extent cutting across the Goliat field is the Troms-Finnmark Fault Complex (TFFC) in the southern margin of the Hammerfest Basin (Figure 1a). The TFFC has a series of listric normal faults (Faleide et al., 1984; Dore, 1995). The Goliat field forms a rollover anticline structure along the TFFC.

The Permian-Triassic boundary is a known regional sequence boundary in the Barents Sea (Figure 2a). In most parts of the Barents Sea, this transition is represented by a change in lithology from Permian carbonates to Triassic siliciclastics. Worsley et al. (1986) attribute this change in lithology from carbonates and evaporate in the Late Palaeozoic to clastic sediments within the Triassic to be related to a combined tectonic and climatic influence. Bugge et al. (1995) identify two different Upper Permian seismic units (representing the Permian-Triassic transition) on the Finnmark platform calibrated to cored wells. The lower seismic unit corresponds to a sharp contact of Triassic siliciclastics to Permian carbonates; meanwhile, the upper seismic transition unit is rather characterized by a transition from Permian matrix supported conglomerates to Triassic siliciclastics.

Late Permian times around the study area saw an influx of coarse clastic sediments sourced from Fennoscandia (Henriksen et al., 2011). In the Goliat field, the transition from the Permian Ørret Formation to the Triassic Havert Formation is a siliciclastic boundary. Shallow stratigraphic cores on the Finnmark platform (east of the Goliat field) from several wells show thick marine anoxic black shales with oil and gas generation potential within the upper Permian succession. This shale unit signals the end of widespread carbonate buildups in the wider Barents Shelf (Henriksen et al., 2011).

The Early Triassic Havert Formation belongs to the Sassendalen Group and was deposited in the study area during the Induan stage (Figure 2a). The other successive lithostratigraphic units within the Sassendalen Group are the Klappmys, Kobbe, and Snadd Formations. According to Henriksen et al. (2011), these four units within the Sassendalen Group represent regional regressive-transgressive cycles in the Southwest Barents Sea. These regressive-transgressive cycles provided the necessary conditions required for the deposition of reservoir, source, and cap rocks, respectively.

A northwest-prograding coastline has been suggested by Worsley (2008) during the Early Triassic, with sediments initially sourced from the Baltic shield and later from the Urals. Palaeogeographic reconstructions of the Triassic in the western Barents Sea according to Glørstad-Clark et al. (2010) also indicate multiple provenance areas but with the main contribution coming from the prograding clastic wedges derived from the collapsing Uralian orogenic belt. Provenance studies (Mørk, 1999) also show a general easterly sediment source area, with a relatively minor contribution from the Fennoscandian shield to the south.

Uplift and exhumation during the Cenozoic times affected wide areas in the entire Barents Sea. Ohm and Karlsen (2008) estimate the amount of uplift in the Goliat to be up to 1500 m using vitrinite reflectance data from wells in the study area. This resulted in overcompaction of the source, reservoir, and caprocks for any given observed depths today.

There is a general fining-upward sequence in the wells with two distinct sand units at the base of the Havert Formation and a very thick shale unit at the top (Figure 3). The gross sand thickness within the Havert Formation in the reference well (7122/7-3) is approximately 120 m. The average PHIE within these sands is approximately 15% and can go up to 25% in the thinner intervals. An arbitrary (west–east) seismic line going through the two available wells is shown in Figure 3a. The reference well is further away from the TFFC, and it is in a structurally lower position compared with the 7122/7-4S well (also shown in Figure 1b). The time slice (Figure 3b) cutting through both sand units clearly shows the main faults (white-dotted lines). The top Permian represented by the Ørret Formation is a very strong negative reflection (Figure 3a and 3b). A drop in impedance is represented by the positive amplitudes and vice versa. Only the reference well has been drilled through the Permian-Triassic boundary (Figure 3c).

Database and methods

A data-driven multidisciplinary workflow has been implemented for porosity and seismic lithology discrimination in the Havert Formation. Carefully proc-

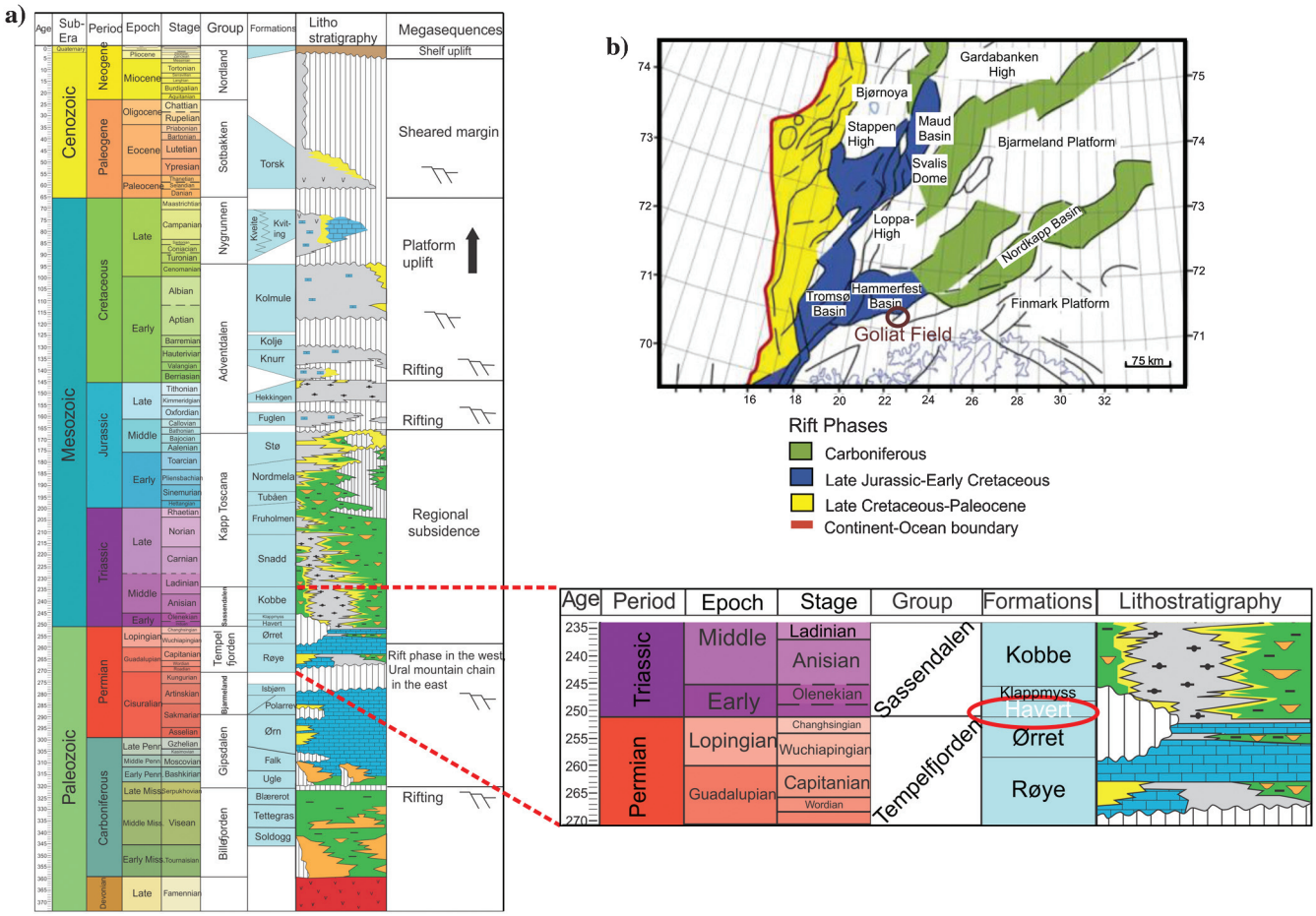

Figure 2. hronostratigraphy of the Norwegian Barents Sea (Glørstad-Clark et al., 2010). The Havert Formation was deposited during the Early Triassic Induan stage. The Permian-Triassic boundary is shown in the red circle. Other hydrocarbon-bearing intervals such as the Snadd, Kobbe, and Klappmys Formations were also deposited during the Triassic Period. (b) The main structural elements in the Western Barents Sea The different colors show the focus of tectonic activity through time (Gabrielsen et al., 1990; Gudlaugsson et al., 1998; Faleide et al., 2008).

essed, high–quality, MAZ 3D prestack and poststack seismic data were available for this study. The input data have been processed in an amplitude variation with offset (AVO)-compliant workflow. For more details on the seismic data acquisition and processing, we refer the reader to Buia et al. (2010). The near-, mid-, and far-partial angle stacks correspond to angles of 17°, 32°, and 45°, respectively.

The S/N estimates for the three partial stacks are computed by taking the Fourier transform of each seismic trace in the target window and performing an autocorrelation with the same trace and adjacent traces. The signal represents the real part of the autocorrelation, and the difference between the autocorrelation and the signal is representative of the noise contribution in the trace. Notice that there is a decrease in the seismic bandwidth with an increasing offset (Figure 4a). The near-stack S/N (approximately 2.2) is larger than the far-stack S/N (approximately 1.90) at 20 Hz. Each of the angle stacks represents MAZ contributions from three (127°, 67°, and 7°N) acquisition azimuths.

A limited well database exists for the Havert Formation in the Goliat field. Only two (7122/7-3 and 7122/7-4S) of the six available exploration wells have been drilled into the Havert Formation. The key input petrophysical logs for the seismic inversion were the S-wave velocity V_S, P-wave velocity V_P, and bulk density ρ_b. The reference well (7122/7-3) has measured V_S and is drilled through the complete Havert Formation. Other standard depth-corrected formation evaluation logs such as gamma ray, PHIE (total porosity minus the clay volume), and V_{sh} have been used to define petrofacies cutoffs. These key log suites are shown in Figure 4b.

Checkshot-corrected V_P logs were used as the input to establish a good seismic-to-well calibration. The well tie was done on the near-stack seismic section (wider bandwidth and lower S/N compared with the larger offset stacks). A 180° phase rotation was applied to a zero-phase statistical wavelet extracted from the near-stack trace, to facilitate visual comparison of the synthetic and actual seismic (Figure 4b). This is because the input seismic has been processed such that positive seismic amplitudes correspond to a decrease in the acoustic impedance. There is a correlation coefficient of approximately 0.8 (Figure 4c) after applying a bulk shift of 6 ms. No further stretch or squeeze operation was necessary.

The methodology used for seismic lithology characterization and porosity prediction (Figure 5) can be summarized into the following main steps:

1) rock-physics feasibility assessment and amplitude variation with angle (AVA) modeling,
2) simultaneous inversion,
3) extended elastic impedance (EEI) inversion,
4) multiattribute regression analysis (MARA),
5) Bayesian sand probability classification.

Rock-physics feasibility and AVA modeling

The main objectives of this step are to (1) explore the relationships between the elastic parameters to PHIE and V_{sh}, (2) establish the best set of elastic parameters

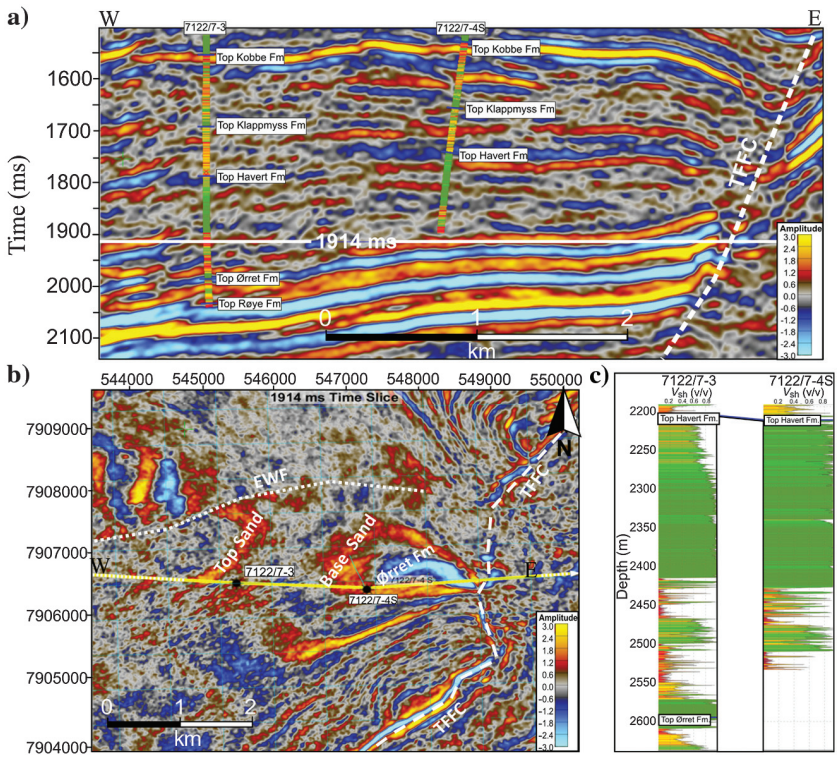

Figure 3. (a) Arbitrary seismic line and (b) time slice showing the top and base Havert sand amplitudes. Positive amplitudes represent a drop in impedance. Some of the faults are shown with the dotted white lines. The green colors on the logs (a and c) indicate shale, and the yellow to red colors highlight the sands.

from the well logs that provide optimum lithology discrimination, and (3) model porosity and fluid perturbations on the seismic AVA response.

The combination of P-impedance (AI) and the ratio of P-wave-to-S-wave velocity (V_P/V_S) is very popular and has been widely used in lithology and fluid discrimination studies. This is desirable because they are readily obtained as end products of prestack inversions. However, the discriminating ability of this attribute pair, like most other lithology and fluid indicators, will vary as a function of burial depth and the prevailing depositional environments even in the same field. As a result, it is important to carry out a feasibility study to determine which set of seismic attributes best discriminate the reservoir zone of interest. Figure 6a and 6b shows a crossplot between AI and V_P/V_S color coded with V_{sh} and PHIE, respectively, for the Havert Formation. The clean sands generally plot with

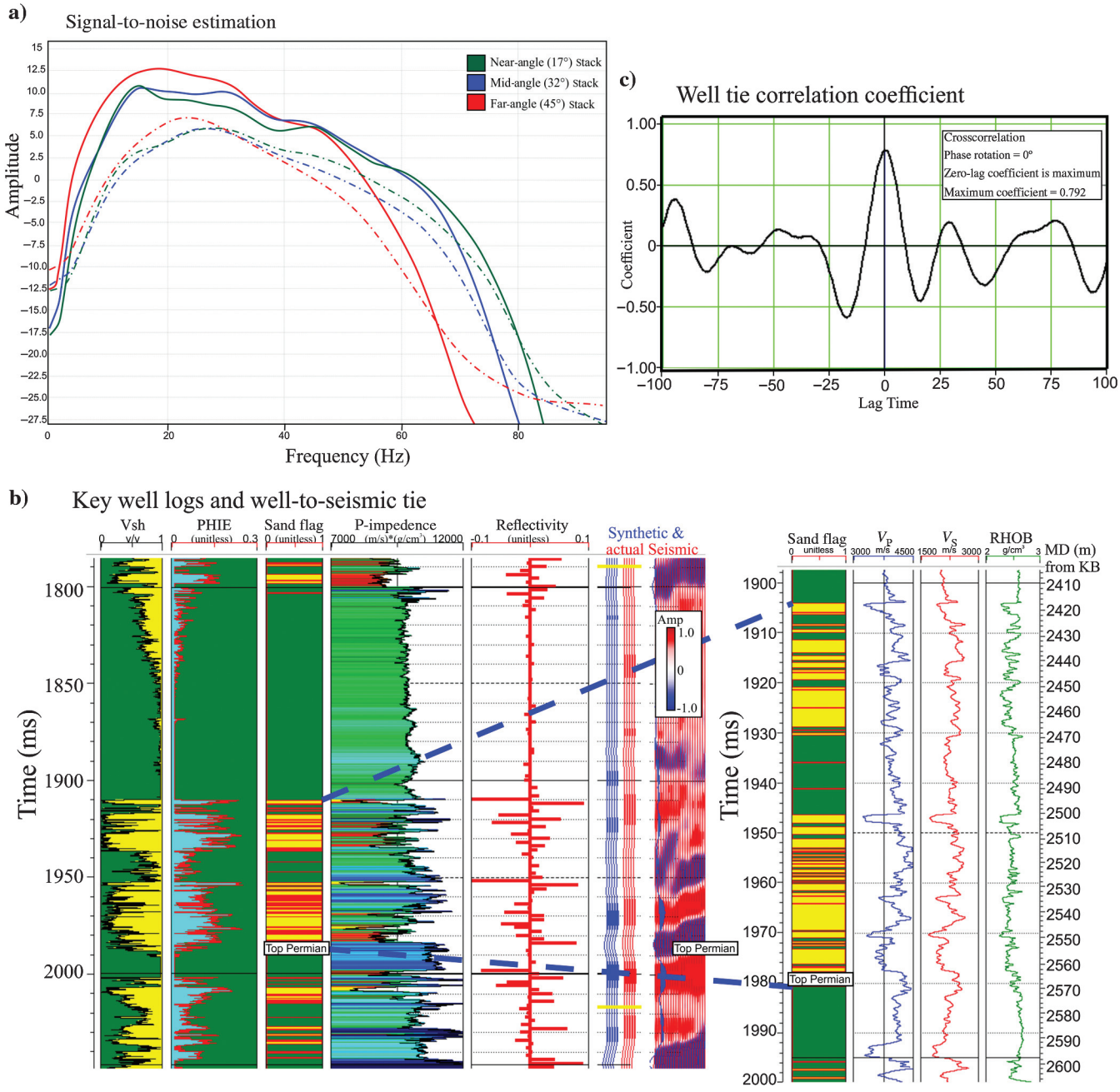

Figure 4. (a) The S/N estimate for the near-, mid-, and far-angle stacks. The solid lines represent the signal, whereas the dotted lines are the estimated noise contributions in each stack over a time window covering the Havert Formation. (b) The key petrophysical logs (in the reference well) used as input to constrain the inversions are shown alongside the seismic well tie. Two distinct sand packages can be seen at the base of the Havert Formation: The synthetic trace is shown in blue, and the actual seismic trace extracted from the well location is shown in red. (c) The correlation coefficient between the synthetic and seismic trace is indicative of the quality of the well tie within the Havert Formation.

low AI (black dotted oval) but with a wide range of V_P/V_S. The mu-rho versus lambda-rho crossplots (Figure 6c and 6d) have better clustering for the cleanest intervals (the black dotted oval) compared with the AI versus V_P/V_S crossplot. However, both are not ideal for lithology discrimination purposes in the Havert Formation because there is no significant trend (overlap between clean and shaly end members) in V_{sh} or PHIE.

EEI log correlations (Figure 7) were then performed to identify the optimum rotation angle (chi angle) required giving the maximum correlation to the PHIE and V_{sh} logs. The optimum chi angles in Figure 7a and 7b formed the basis to run EEI inversions for porosity-tuned impedance [EEI (20°) log] and shale volume-tuned impedance [EEI (25°) log]. The EEI correlation for typical prestack inversion attributes such as mu-rho and V_P/V_S ratio (Figure 7c and 7d) is slightly higher than that for V_{sh} and PHIE.

Figure 8a shows a clear relationship between AI and PHIE color coded by V_{sh}. PHIE has been estimated us-

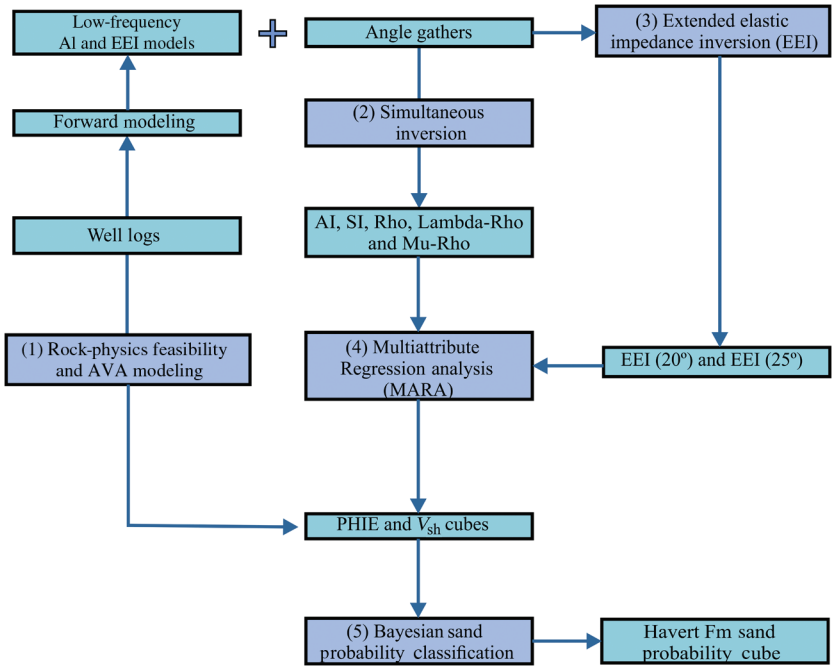

Figure 5. Seismic lithology prediction workflow for the Havert Formation. The main steps are numbered within the appropriate boxes. Three deterministic prestack inversion schemes (steps 2 and 3) are combined in a MARA. Well-derived PDFs are subsequently applied to the output, to generate probability volumes for different petrofacies of interest.

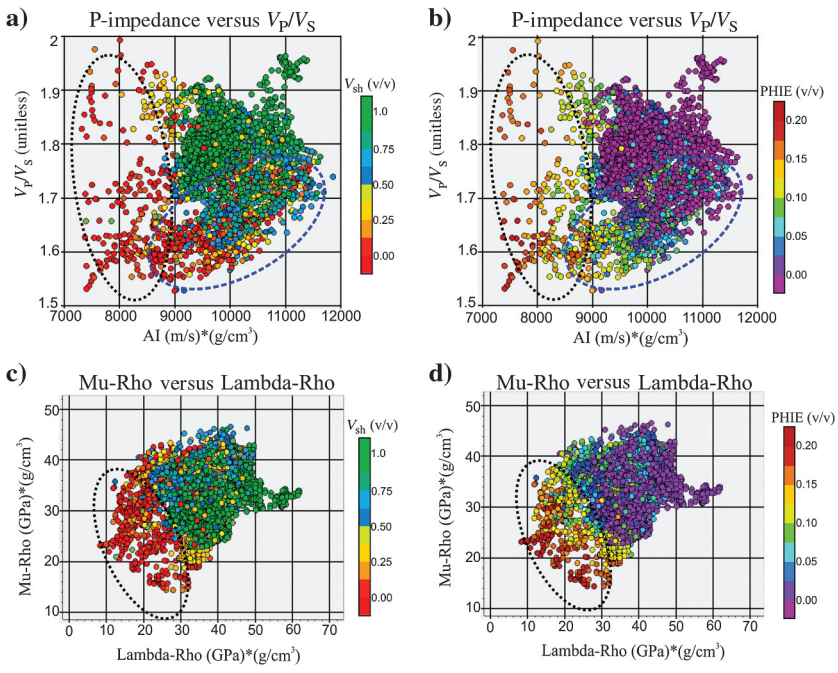

Figure 6. (a and b) The AI versus V_P/V_S crossplots color coded with V_{sh} and PHIE show a poor resolution (wide range) of V_P/V_S for clean sands (dotted black oval). A significant overlap between clean and shaly petrofacies is shown in the dotted blue oval for both figure parts. (c and d) The mu-rho versus lambda-rho crossplots color coded with V_{sh} and PHIE show a better discrimination for the clean sand intervals (dotted black oval) compared with V_P/V_S.

ing the bulk density and V_{sh} log (computed from the gamma ray log). There is also a clear V_{sh} trend (black arrow), which can alternatively be used to define the petrofacies.

Figure 8b shows the corresponding AI versus PHIE plot but in the EEI domain. The color bands can be thought of as individual facies clusters. The crossplots between the PHIE and V_{sh} logs with their respective EEI equivalence (Figure 8c and 8d) show linear trends. Regression lines extracted from the crossplots between the EEI log and the corresponding target log can be used as approximate scaling factors to derive PHIE and V_{sh} from the inverted EEI volumes directly.

A ternary rule-based V_{sh} and PHIE cutoff have been used to define three petrofacies classes, such as clean sand, shaly sand, and shale. Table 1 shows the used petrofacies cutoff criteria and the corresponding petrofacies proportions are shown in Table 2. These cutoffs form the basis for the a priori facies proportions in both wells. The classified log is then crossplotted in different petroelastic domains to identify the best rock-physics training data set. This step ultimately determines the optimum inversion type needed for clean sand discrimination. Probability density functions (PDFs) are then extracted from the best crossplot training data set.

Blocky half-space AVA modeling is a quick interface screening process used to identify the most significant elastic parameter contrasts across an interface. It is also used for the classification of hydrocarbon sands to understand the expected seismic response for other lithology and fluid scenarios not encountered in the reference well. A simplistic AVA 1D-reflectivity modeling of the brine-filled reservoir response was carried out (Figure 9) using Aki and Richards (1980) linearized two-term approximation of the Zoeppritz (1919) equation. Fluid replacement modeling (Gassmann, 1951) was subsequently performed to simulate oil-filled and gas-filled reservoir conditions. Porosity perturbations within the reservoir were also done to understand the effect of compaction or porosity preservation on the resulting AVA response. The corresponding AVA intercept-gradient crossplots for brine, oil, gas, and good average porosity (25%)

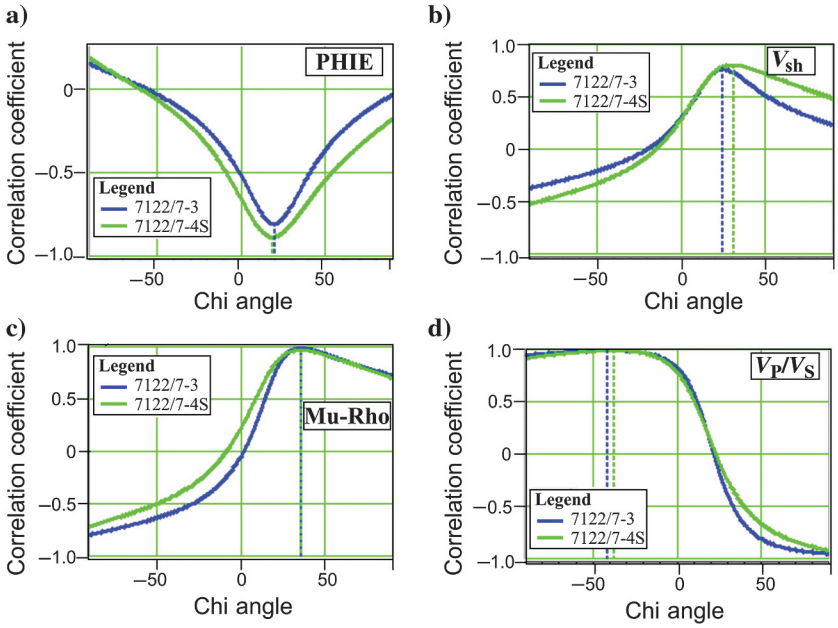

Figure 7. The EEI correlation coefficient to different lithology sensitive parameters. (c and d) The elastic parameters have higher correlation coefficients compared with (a and b) PHIE and V_{sh}, which also show good negative and positive correlations, respectively.

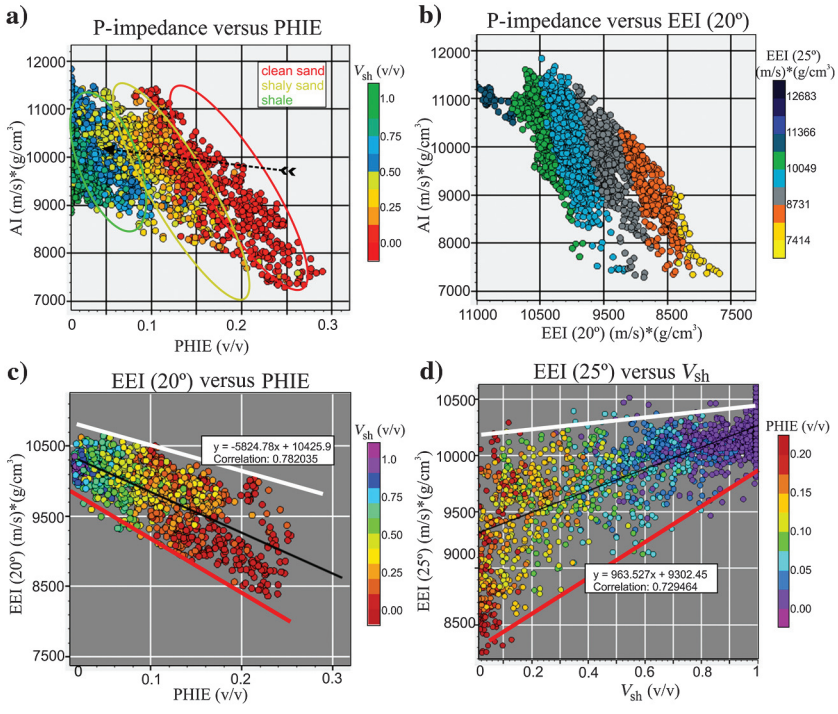

Figure 8. The porosity-impedance relationships and linear regression coefficients linking EEI to porosity and shale volume. (a) The AI versus PHIE crossplot shows a clear trend in V_{sh} (black arrow). The different spheres in (a) represent different facies clusters for clean sand, shaly sand, and shale. The corresponding AI and EEI 20° (PHIE impedance) plot in (b) shows a similar trend in the EEI 25° (V_{sh} impedance). (c and d) The black lines represent the best-fit linear regressions between the parameters. The white and red lines indicate upper and lower bounds, respectively. Notice how these bounds are wider at higher PHIE and lower V_{sh}.

scenarios are used to classify the Havert Formation reservoir sands (Rutherford and Williams, 1989; Castagna et al., 1998).

Simultaneous inversion

Simultaneous inversion is a well-known model-based inversion technique. The simultaneous inversion implementation in this study is based on Hampson et al. (2005). The main objective of this step is to obtain AI, S-impedance (SI), and density (ρ). This can be achieved through several different prestack inversion techniques. However, a simultaneous inversion was chosen so that the background relationship between the output parameters is captured, as opposed to independently inverting for them through a three-term linearized AVO inversion based on Aki and Richards (1980). The quality of the inverted volume is dependent on (1) the quality of the angle stacks, (2) accurate well ties, (3) wavelet processing, and (4) low-frequency background model.

An angle-dependent statistical wavelet was extracted from an inline section along the reference well in the target zone and used as the input for the inversion. The deterministic simultaneous inversion requires a background low-frequency model but for V_P, V_S, and ρ to obtain absolute AI and SI estimates. The interpolation of well-log values away from both wells was guided by stratigraphic horizons. Log-derived linear trends obtained from crossplots between AI to SI and ρ are used as a constraint to guide the inversion (Figure 10). A high-cut 15 Hz filter was equally applied to the output modeled traces. Only the background AI model used in the simultaneous inversion is shown in Figure 11a (background SI and ρ are used but not shown). These background models provide the low-frequency information missing in the band-limited seismic data.

As with all model-based inversions, this initial low-frequency model is then perturbed iteratively to minimize the error between the actual seismic trace and the corresponding inverted seismic traces. The inverted logs are quality checked at the wells to ensure that the inversion honors the well-log data. However, the uncertainty is expected to increase away from the well and in an ideal situation would be verified using a blind well test. Additional lambda-

Table 1. Petrophysical cut-off rules used to define the ternary petrofacies group. The average proportions from the wells are used as the basis for the prior probabilities in the Bayesian facies classification.

Facies name	Petrofacies criteria
Clean sands	VSH = 0.2 & PHIE = 0.2
Shaly sands	0.2 < VSH < 0.5 & 0.1 = PHIE < 0.2
Background shale	0.5 = VSH & PHIE < 0.1

Table 2. Petrophysical cut-off rules used to define the corresponding petrofacies proportions. The average proportions from the wells are used as the basis for the prior probabilities in the Bayesian facies classification.

	7122/7–3	7122/7–4S	Both wells
Clean sands	14.5 %	11.4%	13.0%
Shaly sands	11.2%	6.0 %	8.8 %
Background shale	74.3%	78.9%	76.4%
Unclassified	0.0 %	3.7 %	1.8 %
Number of samples	23720	21415	45135
Pie charts			

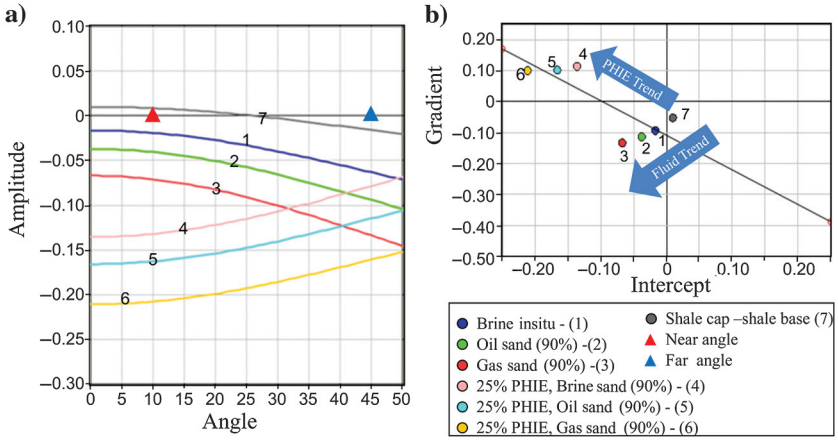

Figure 9. (a) Single-interface blocky AVA modeling for seven scenarios at the top Havert Formation sand in the reference well. Increasing the average porosity causes a change (from positive to negative) in the AVA gradient. The top Havert Formation shale properties are kept constant in the modeling. Orthogonal PHIE and fluid trends are also shown in panel (b).

mu-rho (LMR) attributes (Goodway et al., 1997) are then computed from the inverted volumes.

EEI inversion

The concept of elastic impedance (EI) was first introduced by Connolly (1999). EI is the equivalence of AI for nonzero incidence angles. Some limitations of this concept were later addressed by Whitcombe et al. (2002), and a normalized version of the EI called the EEI was then derived. A standard EEI inversion was done to obtain V_{sh} and PHIE-tuned impedances. The underlying idea is to project the seismic data to specific rotation angles (chi) that emphasize specific reservoir properties of interest such as PHIE and V_{sh} in our case. The chi angle can have values ranging from −90° to +90°.

The optimum chi angles were obtained during the feasibility stage (Figure 7a and 7b). EEI reflectivity (EEIR) volumes are subsequently created using the AVA intercept (A) and gradient (B) as input and applying the corresponding chi rotation angle (α) as shown in equation 1. The statistical wavelets used for the inversion are extracted from the target zone in the EEIR inline sections along the reference well:

$$\mathrm{EEIR} = A\cos\alpha + B\sin\alpha. \tag{1}$$

EEI is also a deterministic inversion and requires a low-frequency background model to obtain absolute EIs. The background models (Figure 11b and 11c) are built by lateral interpolation of the EEI (20°) and EEI (25°) well logs guided by the same smoothened stratigraphic horizons as those used in the simultaneous inversion. The output traces are also passed through a 15 Hz high-cut filter. The filter is implemented so that the high-frequency details in the inversion output should come from the seismic data only. All these volumes are then used as the input for the multilinear regression analysis to predict PHIE and V_{sh}.

Multiattribute regression analysis

The primary objective of this step is to combine all the output volumes from the simultaneous inversion and optionally the EEI inversion into a single analysis

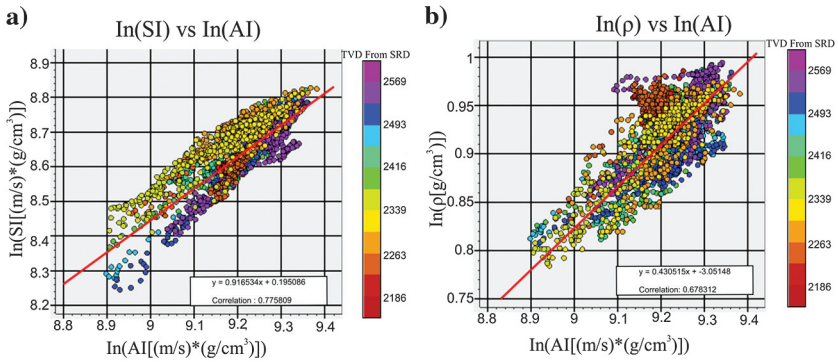

Figure 10. Background linear relationships between the natural logarithms (ln) of AI to SI and density. These background trends are used to constrain the simultaneous inversion solution.

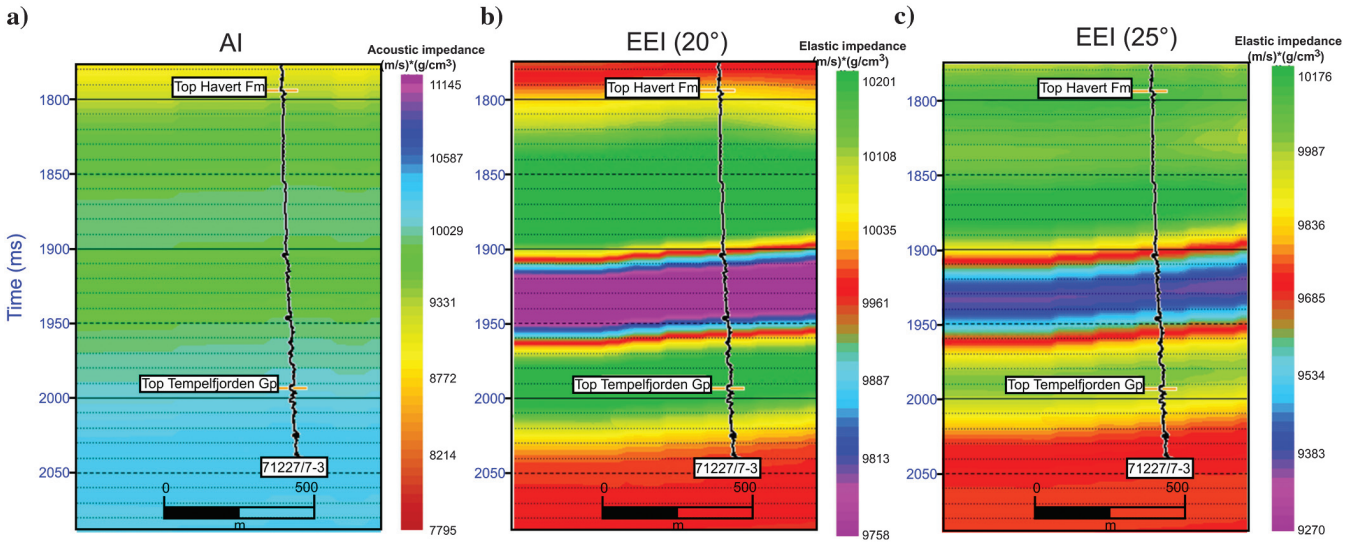

Figure 11. (a) Low-frequency background AI and (b and c) EEI models. A high-cut frequency of 15 Hz has been applied to all the models.

to predict the target logs V_{sh} and PHIE. This is done in two steps: (1) a training process in which the target logs and the seismic attribute volumes are analyzed (by applying a least-squares approach) at both wells to derive a statistical function relating the target logs to the attribute volumes and (2) applying the derived function to create corresponding target log values for each trace in the seismic volume. Several authors have shown the benefits of geostatistical multiattribute transforms to predict porosity and lithology in the seismic volume (Hampson et al., 2001; Pramanik et al., 2004; Calderon and Castagna, 2005).

Again, a good well tie (optimized depth-time curve after check shot correction) is very important because the training process is done when the well logs are recorded in depth. The target logs were resampled at every 4 ms interval to ensure consistency with the seismic processing sample rate of the input data volume. Each of the attributes is initially ranked based on the training error prediction to the target log. This step identifies the best single attribute transform to predict the desired target log. Subsequently, a multiattribute transform is obtained by including the best set of attributes with the least individual prediction error. To avoid over-training the data, a validation error component is incorporated to the analysis. This helps us to decide on the maximum number of attributes to be included in the final training. The final training result is then applied to the entire 3D volume. For more details on multiattribute analysis from seismic attributes, the reader is referred to Russell et al. (1997).

Bayesian sand probability classification

The application of Bayes' theorem in seismic reservoir characterization makes it possible to assign probabilities to any existing knowledge (prior probability), which is used to constrain new evidence. Ezequiel et al. (2016) describe the upside of adding existing geologic knowledge about the area under investigation to constrain the Bayesian facies classification. The new evidence is commonly the output from seismic inversion such as AI and V_P/V_S. However, the particular seismic attribute pair chosen should be based on that which gives the best separation of the facies. In our case, the chosen seismic attribute vector pair was the seismic-derived PHIE and V_{sh} from the MARA. Bayes' theorem is a statement of conditional probability and in our case can be written as

$$\mathrm{P}(\text{clean sand}|\mathrm{PHIE}, V_{sh}) = \frac{\mathrm{P}(\mathrm{PHIE}, V_{sh}|\text{clean sand}) * \mathrm{P}(\text{clean sand})}{\mathrm{P}(\mathrm{PHIE}, V_{sh})}, \quad (2)$$

where $\mathrm{P}(\text{clean sand}|\mathrm{PHIE}, V_{sh})$ is the (posterior) probability of clean sand given PHIE and V_{sh}, P(clean sand) is the prior probability of clean sand, $\mathrm{P}(\mathrm{PHIE}, V_{sh}|\text{clean sand})$ represents the probability of PHIE and V_{sh} are given in a clean sand facies (the likelihood), and $\mathrm{P}(\mathrm{PHIE}, V_{sh})$ is the joint probability of PHIE and V_{sh}. The likelihood is obtained from the PDFs extracted from the well-log training set. The PDFs (non-Gaussian) used are derived by smoothening facies data points in the crossplot space using an operator. An operator length of eight has been used. The longer the operator length, the smoother the PDFs become. The amount of smoothing affects the degree of overlap of the PDFs. Finally, we apply the extracted PDFs and the prior facies proportions obtained from the wells, to the V_{sh} and PHIE seismic volumes. The resulting facies probability cubes are then used as the basis to extract clean sand bodies from which an interpretation of the possible depositional system is inferred.

Results and discussion

Figure 7a shows a strong negative correlation coefficient for PHIE to the EEI curves. As expected, an opposite correlation is seen for the V_{sh}-EEI plot (Figure 7b). The maximum correlation coefficient for PHIE occurs at 20° (chi angle) in both wells. A low EEI (20°) implies a low V_{sh} and high PHIE. Other good lithology indicators such as mu-rho (higher for sand compared with shale) and V_P/V_S ratio (lower values for sand compared with shale) show even stronger positive correlations (Figure 7c and 7d), but in this study, they have been derived from the simultaneous inversion.

A correlation coefficient of approximately 0.8 is observed between the computed EEI (20°) log and PHIE (Figure 8c), whereas a slightly lower correlation of approximately 0.7 is seen between the EEI (25°) log and V_{sh} (Figure 8d) within the Havert Formation. The red, white, and black lines represent approximate lower bounds, upper bounds, and the best-fit regression line, respectively, for the EEI (20°) and EEI (25°) logs. The best-fit regression line can be used to scale the EEI (20°) and EEI (25°) logs to PHIE and V_{sh} units. However, doing it this way, we observe that the uncertainty increases as PHIE increases and V_{sh} decreases. This is important to keep in mind when using a best-fit line for upscaling purposes. These regression lines tend to converge toward lower porosities and higher V_{sh} values. Scaling is very important if the inverted result is to be representative of the absolute porosity and V_{sh} distribution in the area of investigation.

Figure 9 shows the modeled AVA response for the top sand in the Havert Formation in the reference well. The properties of the shale above have been kept constant to help us understand the potential effects of gas and porosity on the AVA response. In Figure 9a, the actual brine conditions in the well show a small negative AVA intercept and gradient (class-II). However, when the sands pinch out, the resulting shale-shale interface gives a positive intercept and a negative gradient (class-IIp). When the in situ brine is substituted with 90% oil and 90% gas using Gassmann's equation, both cases show a corresponding trend of increasing negative AVA intercepts and more negative AVA gradients.

The average porosity in this sand is approximately 15%, but porosities in some thinner intervals can reach

up to 25%. By introducing a 10% increase in the average porosity to represent good sands, the AVA gradients change for all fluid scenarios. There is a change to strong negative AVA intercepts and positive AVA gradients (class-IV). A separation of the AVA classes due to better porosities is shown in the AVA intercept and gradient crossplot (Figure 9b). There is a larger AVA intercept for the good porosity (approximately 25%) gas sands compared with the gas sand scenario with representative average porosities (approximately 15%) in the reference well. This is as expected because for the same pore space distribution, the lower porosity scenario will be stiffer and have reduced fluid sensitivity compared with the higher porosity scenario. The AVA response due to lateral caprock facies variation and organic content has not been modeled but will play an important role as well (Hübert et al., 2006). This effect should be evaluated on a case-by-case basis.

Figure 12 shows the inversion quality control at the reference well. A good result is obtained by maximizing the correlation between the inverted logs and the actual logs and minimizing the error between the inverted traces and the input seismic traces. For the simultaneous inversion (Figure 12a), the inverted V_P/V_S and ρ outputs capture the general vertical trends in the logs except in the inverted ρ log between 1900 ms. The wavelet time and frequency response for the angle dependent wavelet used in the simultaneous inversion are shown in Figure 12b. Applying a single transform to obtain PHIE from this result will result in erroneous values especially at less than 1900 ms. The simultaneous inversion error (approximately 0.24) is smaller than the inversion error (approximately 0.4) obtained from the EEI 25° and EEI 20° inversions (Figure 12c and 12d). The inversion errors for the EEI inversions are relative to the EEIR traces, whereas that for the simultaneous

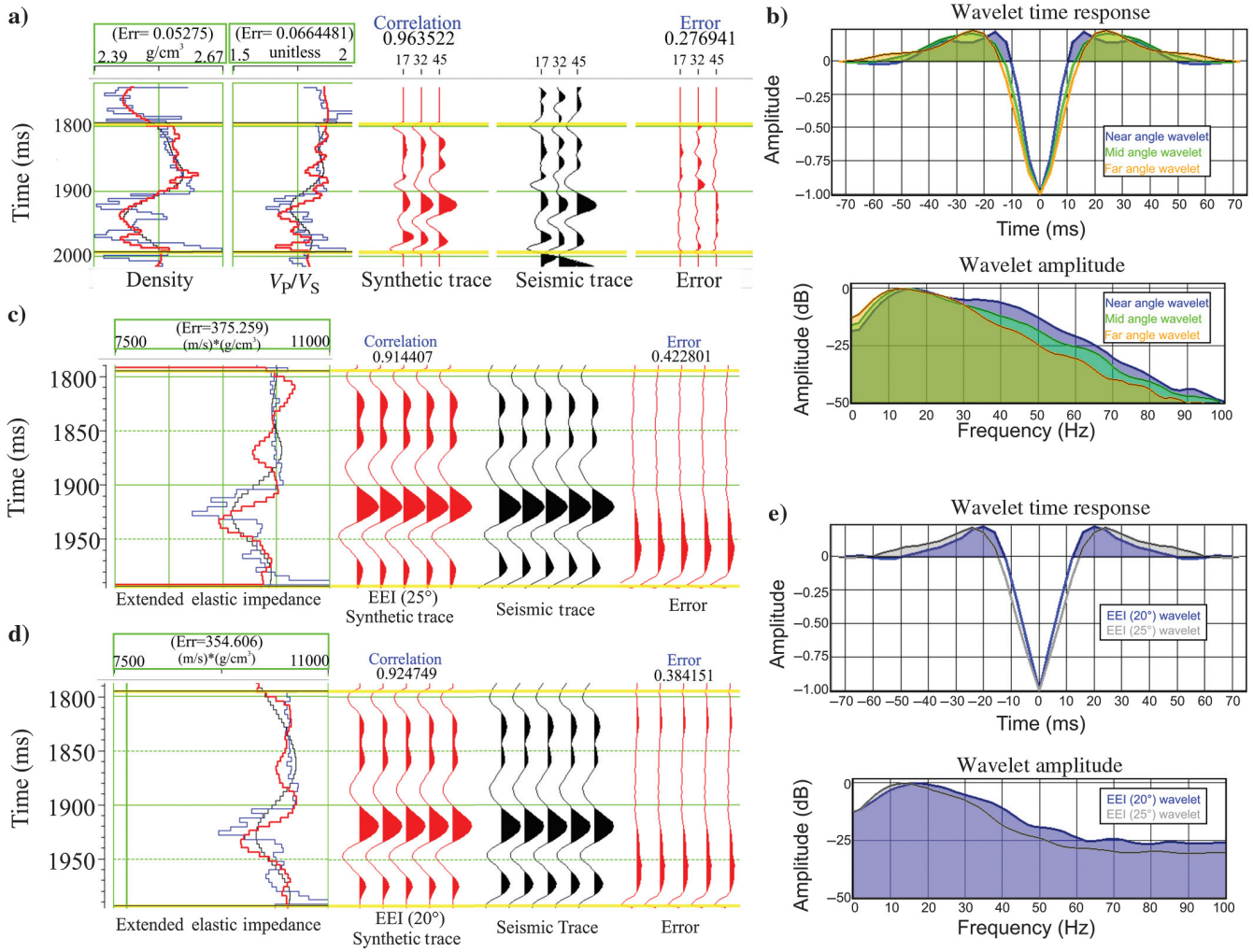

Figure 12. Inversion quality control at the reference well by comparing the inversion-derived synthetic seismic traces at the well location with the seismic trace extracted at the well location. (a) The simultaneous inversion has the lowest error followed by (d) the EEI (20°) inversion, and last by (c) the EEI (25°) inversion result. (b) The angle-dependent statistical zero-phase wavelet used for the simultaneous inversion and (e) the EEI wavelets are shown for visual comparison. (e) The EEI wavelets are extracted from their respective chi angle-rotated EEIR traces.

inversion is relative to the input angle gathers. Figure 12e shows that the EEI 20° wavelet has a slightly larger bandwidth relative to the EEI 25° wavelet.

Despite the vertical resolution limitations in the inverted results from both prestack inversions, the general vertical trends were considered good enough for further multiattribute analysis to estimate V_{sh} and PHIE.

A multilinear regression attribute analysis provides a nice way of integrating a group of related seismic attributes. To show the benefit of integrating both prestack inversions into a single analysis, the output from the simultaneous inversion and the derived LMR attributes were first used as separate training data set. This training data set was then optimized using the EEI inverted seismic traces in the training process instead of the zero-offset seismic trace.

Figure 13 shows the resulting error profiles during the training phase for V_{sh} with an increasing number

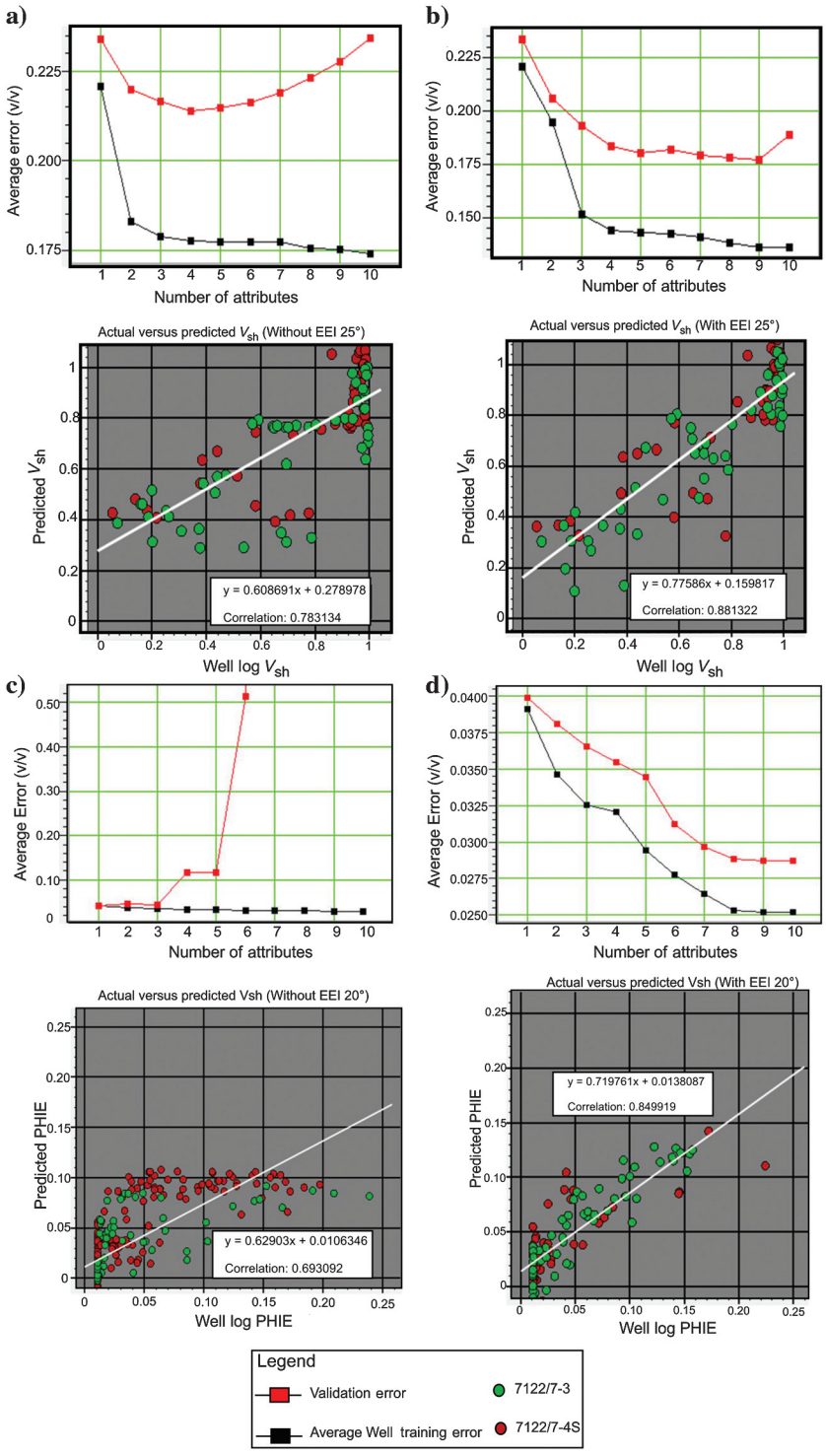

Figure 13. MARA for V_{sh} and PHIE prediction, with and without EEI (25°) and EEI (20°), respectively. The average training (black curve) and validation errors (red curves) are shown for all four scenarios alongside the corresponding predicted V_{sh} and PHE. Notice (b and d) the reduction in the validation errors in cases in which EEI (25°) and EEI (20°) are added to the training set. There is a corresponding increase in the correlations between the predicted V_{sh} and PHIE to the actual logs (b and d) compared with (a and c) scenarios in which no EEI trace was included in the training.

of attributes included in the training process. There are two types of errors represented: (1) the average training error (black curve) that shows a net decreasing trend by combining successive attributes in the classification and (2) the validation error (red curve) that tends to increase after a given number of attributes are used in the classification. The specific attribute transforms used for PHIE and V_{sh} are listed in Tables 3 and 4, respectively. The average training error decreases using all 10 attributes in Figure 13. However, the validation error increases progressively after the fourth attribute (Figure 13a) in the training set for predicting V_{sh} without incorporating the EEI (25°) trace. Meanwhile, the validation error increases significantly only after the ninth attribute when the EEI (25°) seismic trace is included in the analysis. This implies that adding more than four attributes in Figure 13a reduces the prediction ability of V_{sh} in the training result. This is because the validation involves "hiding" one of the wells and then estimating the result with an operator calculated from the other well. An increase in the validation error therefore implies that the target log is being overclassified. The predicted results in Figure 13a and 13b show a corresponding approximately 10% improvement in the correlation coefficient between the predicated V_{sh} to the actual V_{sh} by introducing a V_{sh}-tuned EEI (25°) seismic trace in the analysis.

Similar observations are made for the PHIE analysis. The validation error starts to increase soon after the third attribute (Figure 13c) when the EEI (20°) inverted trace is not included in the analysis. There is a significant increase in the correlation between the predicted PHIE and actual PHIE (Figure 13d) when the EEI (20°) trace is used in the training compared with Figure 13c.

The final predicted V_{sh} and PHIE logs are obtained by applying up to the ninth attribute transform in Tables 3 and 4. The average correlation between the final predicted V_{sh} and PHIE to the actual well logs is approximately 80%.

Figure 14 compares the inverted logs with actual logs at the well location for the three prestack inversion results with the predicted results from the MARA. The typical output from a simultaneous inversion is AI, SI, and ρ. The V_P/V_S ratio can be obtained by taking the ratio of AI to SI. The density term requires good-quality long-offset data (the mid-angle for the far-angle stack used for this purpose was 45°). The logs have been resampled at a 4 ms interval (the same as the seismic processing sample rate of the input data). The sand flag is shown in yellow in track 1. Tracks 4 and 5 in Figure 13 show a comparison between the inverted ρ and V_P/V_S logs with the actual logs resampled at 4 ms intervals. Notice also that the inverted density log is unable to resolve the shale unit (track 1) within the green rectangle, and it follows the low-density trend of the sands above and below the shale interval. The inverted V_P/V_S log captures the trends in the actual log better than the density term.

The results from the EEI inversion in Figure 14 (tracks 6 and 7) capture the general vertical log trends, but they still lack the resolution to pick up the interbedded sand and shale trends. The shale unit within the green rectangle is completely missed by the inverted logs from both inversions, and it is out of phase with the actual logs. This implies that using the EEI (20°) and EEI (25°), logs directly in this case will indicate the relative vertical trends of PHIE and V_{sh} in the data but will not be adequate for sand prediction using well-derived PDFs.

Figure 14 shows the final predicted V_{sh} and PHIE logs in blue, compared with the actual V_{sh} and PHIE logs in

Table 3. Final multiattribute transforms used in the training process to condition V_{sh}. The successive error is obtained by applying all the attributes preceding it.

1	1/(inverted rho)	0.221118	0.234172
2	Filter 15/20–25/30	0.195223	0.206241
3	(Inverted AI^2)	0.152004	0.193538
4	Amplitude weighted frequency	0.144393	0.183895
5	Second derivative instantaneous amplitude	0.143207	0.180935
6	Filter 55/60–65/70	0.142724	0.182373
7	Apparent polarity	0.141073	0.179948
8	Filter 35/40–45/50	0.138646	0.178743
9	Filter 45/50–55/60	0.136752	0.177515
10	Second derivative	0.136608	0.189384

Table 4. Final multiattribute transforms used in the training process to condition PHIE. The successive error is obtained by applying all the attributes preceding it.

1	1/(inverted rho)	0.039190	0.039934
2	1/(inverted mu-rho)	0.034691	0.038163
3	Derivative	0.032614	0.036618
4	Filter 5/10–15/20	0.032146	0.035522
5	Quadrature trace	0.029483	0.034516
6	Apparent polarity	0.027819	0.031307
7	Derivative instantaneous amplitude	0.026504	0.029730
8	Filter 15/20–25/30	0.025361	0.028896
9	Cosine instantaneous phase	0.025273	0.028777
10	Average frequency	0.025272	0.028776

red (track 1). The white curves shown in tracks 2 and 3 are the predicted results for PHIE and V_{sh} without incorporating the EEI inversion output in the workflow. The initially poorly resolved shale unit below 1900 ms (within the green rectangle) is now well-resolved in the final result compared with either of the inversion results independently or the combined training result without the EEI attributes (white curve). This clearly shows the benefit of integrating different methods into a single workflow. The V_{sh} and PHIE volumes from the training result are then used as input for Bayesian sand probability estimates in the Havert Formation.

The V_{sh} and PHIE arbitrary lines along the wells (Figure 15a and 15b) show a generally better PHIE and lower V_{sh} at the deeper sand compared with the shallower sand in the reference well. The sand flag (yellow for sand) is plotted along the wells for a visual quality control. The top thick shaly part of the Havert Formation is captured in the V_{sh} and PHIE sections. The lower Havert sand also shows a better lateral connectivity in addition to a better predicted V_{sh} and PHIE. There is an increase in V_{sh} and a corresponding decrease in PHIE at this stratigraphic time level toward the 7122/7-4S well. The same arbitrary line shows an inverse correlation between PHIE and V_{sh} as expected. For shallower unconsolidated sands, this would potentially be more ambiguous because the depositional porosity of shales is usually higher than that of sands. This would result in high V_{sh} intervals also correlating with good PHIE. However, this is not the case for the Havert Formation in this study area, which has been buried even deeper than present-day depths before the major uplift in Cenozoic times (Faleide et al., 1993). In addition, the input PHIE logs used in the training process had been corrected for the clay volume.

The extracted PDFs of each petrofacies class from the PHIE and V_{sh} well logs are shown in Figure 16a. PDFs from the upscaled well log and the volume trace are also extracted (not shown) and are used to model the probability of each petrofacies at the reference well in Figure 16b.

The modeled probability tracks show a good correlation for the shale probabilities from the well data and composite traces extracted at the well location. This implies that using a binary classification of sand and shale would be adequate even for the volume trace. Note the decrease in the vertical resolution of the classified logs due to upscaling. The thin clean sands at approximately 1940 ms would be completely missed out in the composite trace, if the PDFs from the composite volume trace are used in this ternary facies classification.

Figure 16c shows the confusion matrix resulting from the extracted PDFs using the well logs, upscaled

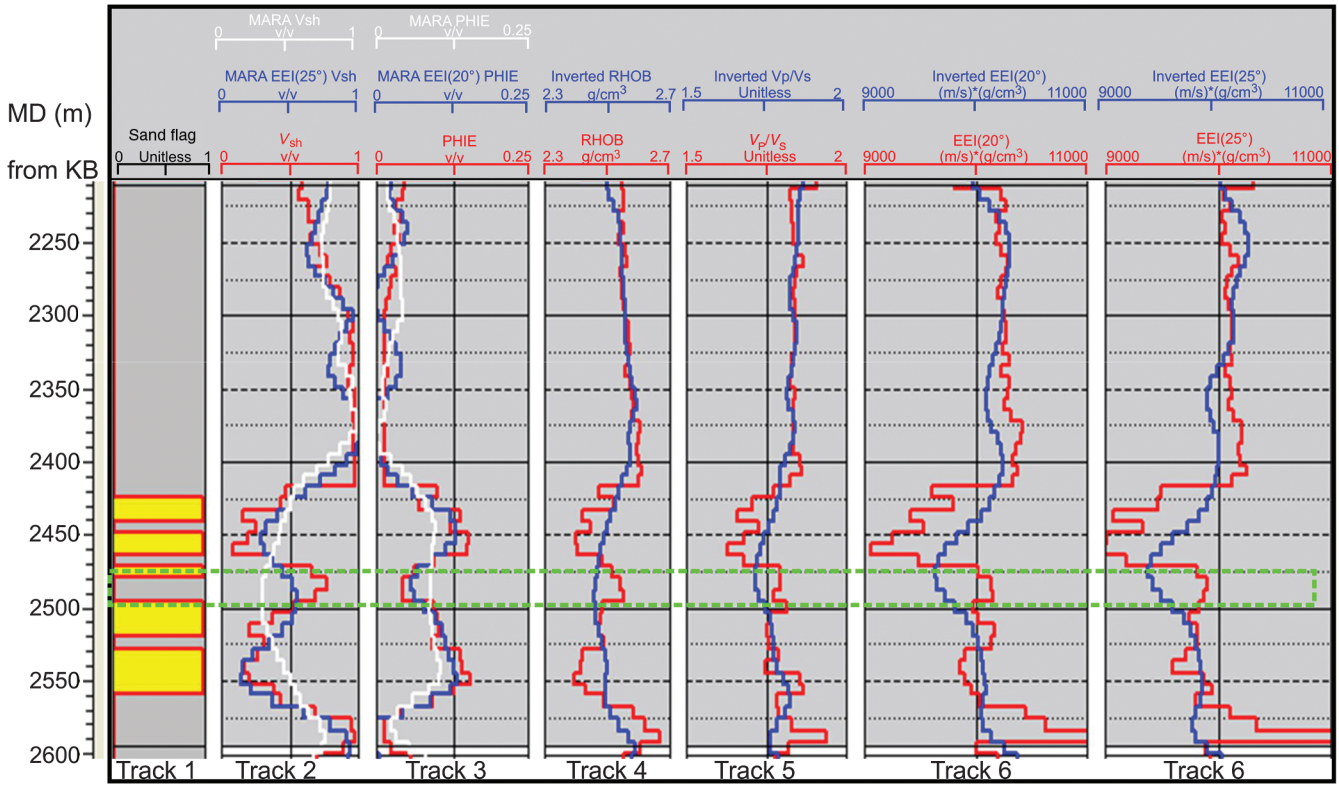

Figure 14. Comparisons between the resampled (4 ms) actual well logs (red) and the inverted logs (blue). Both EEI logs in tracks 6 and 7 capture the general vertical trends but are out of phase compared with the actual logs. The low density and high V_P/V_S shale interval (Track 1) within the dotted green rectangle are missed by the simultaneous inversion results in tracks 4 and 5, respectively. Notice the improvement in the dotted white rectangle region in tracks 2 and 3. The white curves represent the predicted PHIE and V_{sh} when the EEI (20°) and EEI (25°) traces are not used to augment the training set for the MARA.

logs, and a composite seismic trace extracted at the well location. Diagonal values in the confusion matrix indicate the success of the classification at the well location. For example, clean sands are misclassified as shaly sands approximately 4%, 36%, and 80% of the time using the well logs, upscaled logs, and the composite seismic, respectively. The degree of misclassification increases by upscaling the training data set. PDFs from the well logs have been selected as the best training set and are applied to the V_{sh} and PHIE composite volume.

The spatial property variations and continuity of the cleaner and better connected lower sand unit are better seen from horizon slices in Figure 17. The horizon slices from the simultaneous inversion (Figure 17a), EEI inversions (Figure 17b and 17c), and the Bayesian classification result (Figure 17d) are compared with each other. In terms of the lateral resolution, the AI horizon slice is ranked the least followed by the V_P/V_S ratio slice (Figure 17a). However, the PHIE horizon slice shows the best resolution followed by the V_{sh} slice (Figure 17c). In general, low AI areas largely correspond to low V_P/V_S and V_{sh}.

A fan-shaped geometry can be seen on these maps in Figure 17. Based on the seismic geomorphological character of this interval, we infer a point sourced sedimentation for the sands on the hanging wall of the TFFC. This fan-shaped geometry is structurally constrained by the two branches of the TFFC. One of the interpreted feeder channels of the fan complex is clearly seen from the PHIE horizon slice. This apparent syndepositional relationship may be indicative of some minor fault activity in the Early Triassic in the southwestern part of the Barents Shelf. However, more detailed structural analysis is required to support this claim.

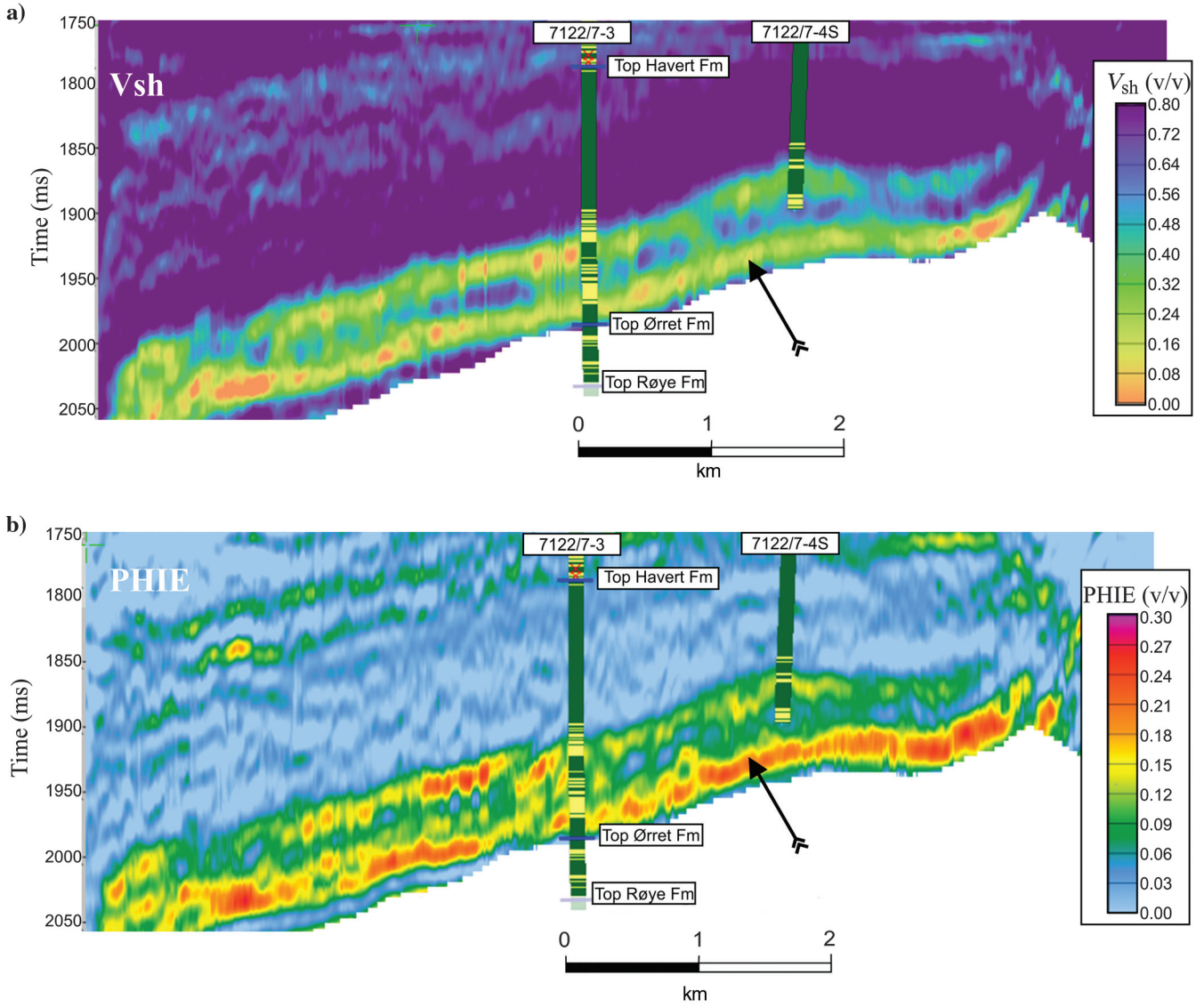

Figure 15. Arbitrary line sections for (a) V_{sh} and (b) PHIE. The base sand layer (indicated with the arrow) shows higher PHIE, lower V_{sh}, and better continuity. The sand flag for the wells is also plotted with yellow indicating sand.

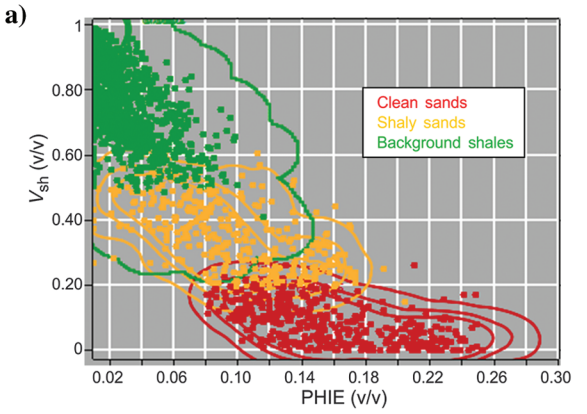

c)

Classified log

Litho-log: Well log	Clean sands	Shaly sands	Background shale
Clean sands	95.99 %	4.00 %	0.02 %
Shaly sands	8.20 %	83.20 %	8.60 %
Background shale	0.00 %	0.60 %	99.40 %

Classified log

Litho-log: Upscaled log	Clean sands	Shaly sands	Background shale
Clean sands	50.00 %	35.71%	14.29 %
Shaly sands	20.00 %	40.00 %	40.00 %
Background shale	2.99 %	1.49 %	95.52 %

Classified log

Litho-log: Volume trace	Clean sands	Shaly sands	Background shale
Clean sands	13.33 %	80.00 %	6.67 %
Shaly sands	20.00 %	40.00 %	40.00 %
Background shale	0.00 %	13.64 %	86.36 %

Figure 16. (a) The crossplot between V_{sh} and PHIE color coded with the different petrofacies. The green represents shale, orange is for shaly sand, and red is for clean sands. The corresponding PDFs (lines) for the different classes are also displayed using a smoothing of eight. (b) The modeled petrofacies probability tracks using different training sets are shown. The volume trace shale probability is consistent with both well logs but lacks the finer detail. (c) A confusion matrix comparison for the well logs, upscaled log, and the composite volume trace extracted at the well location is also shown. The diagonal elements in the confusion matrix represent the degree of success in the classification; meanwhile, off-diagonal elements show the error between the actual log and the classified log. The well logs have been selected as the best training set.

Figure 17d shows the probability of clean and shaly sands within the lower sand unit in the Havert Formation. Based on the contour overlay on these maps, there is a higher probability of clean sands in structurally lower positions around the 7122/7-3 well compared with structurally higher positions closer to the TFFC. A corresponding higher probability of shaly sands is observed on structurally higher positions around the 7122/7-4S well within the same stratigraphic interval.

Clean sand bodies have been extracted from the volume using a 90% clean sand probability cutoff. The 3D result of the extraction is shown in Figure 17d together with the vertical and horizontal slices of V_P/V_S ratios from the simultaneous inversion. Based on the extracted clean sand bodies, two fan lobes can be distinguished. The main lobe (lobe A) has a northeast–southwest orientation, and it has the main feeder channel. This feeder channel is better seen by looking at the high PHIE trend in the southern part of Figure 17c. The subsidiary lobe (lobe B) has lower porosities and is separated from the main lobe by an east–west fault (EWF in Figure 3). The apparent clean sand depositional bypass from structurally higher positions close to the TFFC to structurally lower positions may be explained by a local sediment supply sourced from the hanging wall of the TFFC. Coarser clastic material is first supplied during fault movement. The supply of local coarse clastic material is expected to reduce over time as the movement along the fault dies out. This may potentially explain the shaly sand observation close to the apex of the fan complex.

Conclusion

The suggested methodology integrates existing industry standard techniques for lithology screening. The in situ low porosity brine-filled top Havert Formation sands show a class-II AVA response. Blocky AVA modeling showed that high porosities would change the AVA class for low-porosity Havert Formation sands to a class-IV AVA response irrespective of the pore fluid. This has implications for any Havert Formation prospects with better average porosities than that observed in the Goliat area. Model-based inversions are very dependent on the background model, which can be an important source of error in the output. A better result will be obtained if more wells are available to constrain the low-frequency model. However, by integrating a multilinear attribute regression analysis and a quantitative sand probability estimate, we are able to narrow down the risk. There is an improvement in the predicted V_{sh} and PHIE by approximately 10% when the EEI results are integrated into the MARA. The PHIE result showed the best lateral resolution of the clean sands compared with the prestack inversion results and the V_{sh} attribute. The output volumes can be used to guide petrophysical reservoir models and can potentially aid in the ranking of drilling targets based on the extracted sand bodies.

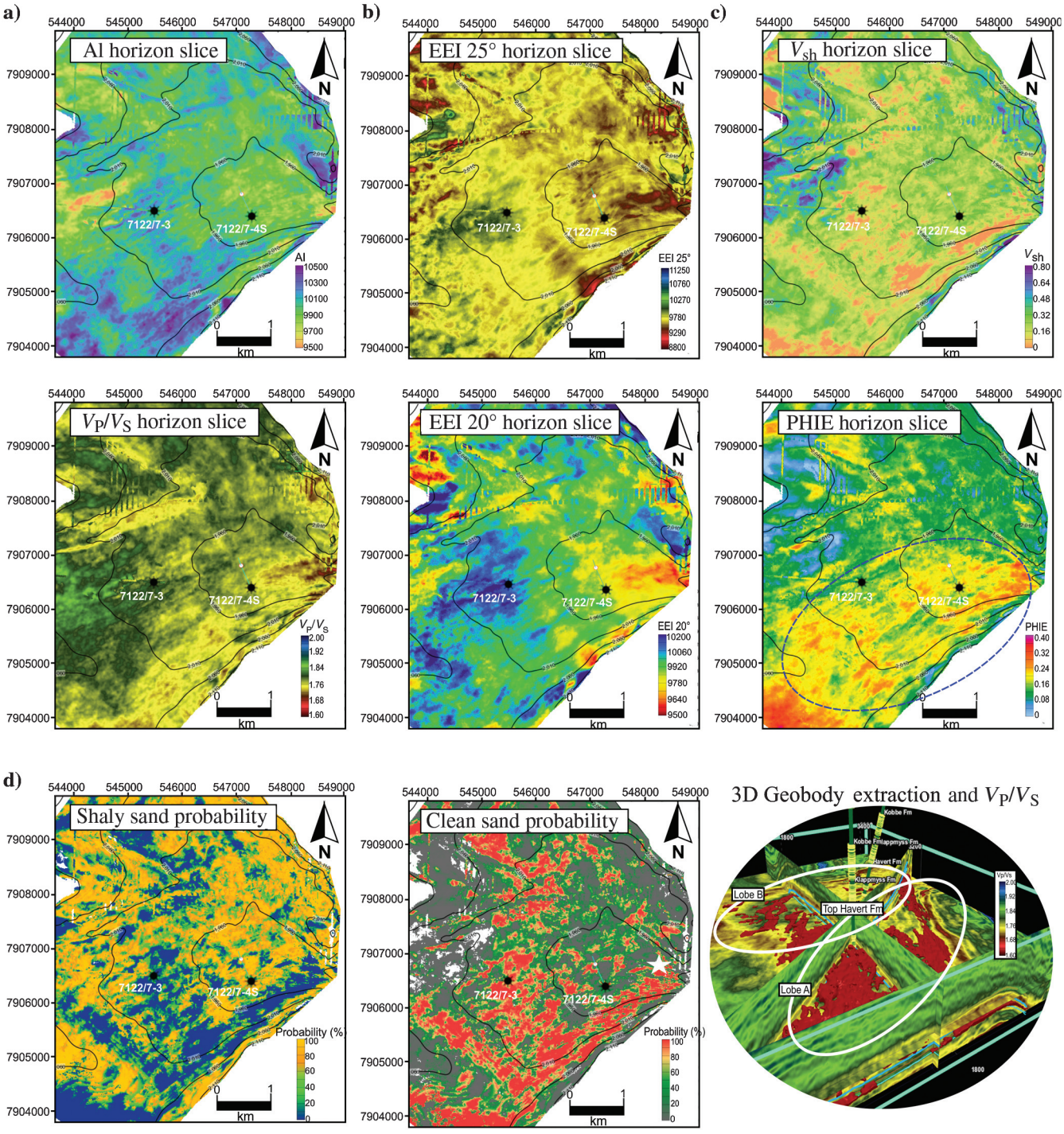

Figure 17. Horizon slices extracted from the base sand (arrow in Figure 14) showing the differences in the spatial resolution. (a) The simultaneous inversion result, (b) the EEI result, (c) the multiattribute regression result, and (d) the Bayesian classification for shaly and clean sands. (c) The PHIE slice shows the best resolution with the main feeder channels to the south within the blue dotted oval. (d) The probability of clean sands is seen to be less close to the apex of the fan (white star) around the 7122/7-4S well. The extraction window is approximately 10 ms. A 3D view of the extracted sand bodies (red) based on a 90% cutoff on the clean sand probability cube is also shown. The seismic lines displayed are V_P/V_S with green colors representing dominantly shaly intervals and yellow to red colors indicating sand. The sand flag from both wells is also included for visual quality control.

To successfully apply this method for different depth intervals, statistical modeling of the elastic parameter depth trends is required. The PDFs extracted from the well also need to be stochastically modeled for the different depths of investigation. More detailed structural studies are required to ascertain and constrain the timing of the suggested fault movement along the TFFC in the earliest Triassic times.

Acknowledgments

This work is (partially) funded by the project "Reconstructing the Triassic Northern Barents Shelf: basin infill patterns controlled by gentle sags and faults" (Triass North) under grant no. 234152 from the Research Council of Norway (RCN) and with financial support from Tullow Oil Norge, Lundin Norway, Statoil Petroleum, Edison Norge, and DEA Norge. The authors also thank Eni Norge and Statoil ASA of the PL229 license for permission to publish the data. This work has been carried out using Hampson-Russell, RokDoc, and DUG Insight commercial software packages at the University of Oslo.

References

Aki, K., and P. G. Richards, 1980, Quantitative seismology: Theory and methods: Freeman.

Bugge, T., G. Mangerud, G. Elvebakk, A. Mørk, I. Nilsson, S. Fanavoll, and J. O. Vigran, 1995, The Upper Paleozoic succession on the Finnmark Platform, Barents Sea: Norsk Geologisk Tidsskrift, **75**, 3–30.

Buia, M., C. Cirone, J. Leutscher, S. Tarran, and B. Webb, 2010, Multi-azimuth 3D survey in the Barents Sea: First Break, **28**, 65–69.

Calderon, J. E., and J. Castagna, 2005, Porosity and lithologic estimation using rock physics and multiattribute transforms in the Balcon field, Colombia — South America: 75th Annual International Meeting, SEG, Expanded Abstracts, 444–447, doi: 10.1190/1.2142237.

Castagna, J., H. Swan, and D. Foster, 1998, Framework for AVO gradient and intercept interpretation: Geophysics, **63**, 948–956, doi: 10.1190/1.1444406.

Connolly, P., 1999, Elastic impedance: The Leading Edge, **18**, 438–452, doi: 10.1190/1.1438307.

Dario, G., E. P. S. Mancini, and C. Tarchiani, 2013, Seismic driven probabilistic classification of reservoir facies for static reservoir modelling: A case history in the Barents Sea: Geophysical Prospecting, **61**, 613–629, doi: 10.1111/j.1365-2478.2012.01115.x.

Dore, A. G., 1995, Barents Sea geology, petroleum resources and commercial potential: Arctic, **48**, 207–221, doi: 10.14430/arctic1243.

Ezequiel, F. G., S. Gesbert, and R. Hofmann, 2016, Adding geologic prior knowledge to Bayesian lithofluid facies estimation from seismic data: Interpretation, **4**, no. 3, SL1–SL8, doi: 10.1190/INT-2015-0220.1.

Faleide, J. I., S. T. Gudlaugsson, and G. Jacquart, 1984, Evolution of the western Barents Sea: Marine and Petroleum Geology, **1**, 123–150, IN1–IN4, 129–136, IN5–IN8, 137–150, doi: 10.1016/0264-8172(84)90082-5.

Faleide, J. I., F. Tsikalas, A. J. Breivik, R. Mjelde, O. Ritzmann, Ø. Engen, J. Wilson, and O. Eldholm, 2008, Structure and evolution of the continental margin off Norway and the Barents Sea: Episodes, **31**, 82–91.

Faleide, J. I., E. Vågnes, and S. T. Gudlaugsson, 1993, Late Mesozoic-Cenozoic evolution of the southwestern Barents Sea, *in* J. R. Parker, ed., Proceedings of the 4th Conference on Petroleum Geology of Northwest Europe, The Geological Society of London, 933–950.

Gabrielsen, R. H., R. B. Færseth, L. N. Jensen, J. E. Kalheim, and F. Riis, 1990, Structural elements of the Norwegian Continental Shelf Part 1 — The Barents Sea Region: NPD-Bulletin, **6**, 33.

Gassmann, F., 1951, Elastic waves through a packing of spheres: Geophysics, **16**, 673–685, doi: 10.1190/1.1437718.

Glørstad-Clark, E., J. I. Faleide, B. A. Lundschien, and J. P. Nystuen, 2010, Triassic seismic sequence stratigraphy and paleogeography of the western Barents Sea area: Marine and Petroleum Geology, **27**, 1448–1475, doi: 10.1016/j.marpetgeo.2010.02.008.

Goodway, B., T. Chen, and J. Downton, 1997, Improved AVO fluid detection and lithology discrimination using Lamé petrophysical parameters, λρ, μρ, and λ/μ fluid stack, from P and S inversions: National Convention, CSEG, **22**, 183–186.

Gudlaugsson, S. T., J. I. Faleide, S. E. Johansen, and A. J. Breivik, 1998, Late Paleozoic structural development of the South-western Barents Sea: Marine and Petroleum Geology, **15**, 73–102, doi: 10.1016/S0264-8172(97)00048-2.

Hampson, D. P., B. H. Russell, and B. Bankhead, 2005, Simultaneous inversion of pre-stack seismic data: 75th Annual International Meeting, SEG, Expanded Abstracts, 1633–1636.

Hampson, D. P., J. S. Schuelke, and J. A. Quirein, 2001, Use of multiattribute transforms to predict log properties from seismic data: Geophysics, **66**, 220–236, doi: 10.1190/1.1444899.

Henriksen, E., A. E. Ryseth, G. B. Larssen, T. Heide, K. Rønning, K. Sollid, and A. V. Stoupakova, 2011, Tectonostratigraphy of the greater Barents Sea: Implications for petroleum systems: Geological Society, London, Memoirs 35, 163–195.

Hübert, L., K. Müller, and A. Selnes, 2006, Improving AVO modeling using geological knowledge, 4 examples from the Norwegian Continental Shelf: 76th Annual International Meeting, SEG, Expanded Abstracts, 259–263, doi: 10.1190/1.2370061.

Johansen, S. E., B. K. Ostisty, Ø. Birkeland, O. Cristensen, S. I. Cheredeev, E. A. Ignatenko, and M. Margulis, 1993, Hydrocarbon potential in the Barents Sea region: Play distribution and potential, *in* T. O. Vorren, E. Bergsager, Ø. A. Dahl-Stamnes, E. Holler, B. Johansen, E. Lie, and T. B. Lund, eds., Arctic geology and petroleum potential, NPF Special Publication: Elsevier, 273–320.

Mørk, M. B. E., 1999, Compositional variations and provenance of Triassic sandstones from the Barents Shelf: Journal of Sedimentary Research, **69**, 690–710, doi: 10.2110/jsr.69.690.

Ohm, S. E., and D. A Karlsen, 2008, Geochemically driven exploration models in uplifted areas: Examples from the Norwegian Barents Sea: AAPG Bulletin, **92**, 1191–1223, doi: 10.1306/06180808028.

Pramanik, A. G., V. Singh, R. Vig, A. K. Srivastava, and D. N. Tiwary, 2004, Estimation of effective porosity using geostatistics and multiattribute transforms: A case study: Geophysics, **69**, 352–372, doi: 10.1190/1.1707054.

Russell, B., D. Hampson, J. Schuelke, and J. Quirein, 1997, Multiattribute seismic analysis: The Leading Edge, **16**, 1439–1444, doi: 10.1190/1.1437486.

Rutherford, S., and R. Williams, 1989, Amplitude-versus-offset variations in gas sands: Geophysics, **54**, 680–688, doi: 10.1190/1.1442696.

Whitcombe, D. N., P. A. Connolly, R. L. Reagan, and T. C. Redshaw, 2002, Extended elastic impedance for fluid and lithology prediction: Geophysics, **67**, 63–67, doi: 10.1190/1.1451337.

Worsley, D., 2008, The post-Caledonian development of Svalbard and the western Barents Sea: Polar Research, **27**, 298–317, doi: 10.1111/j.1751-8369.2008.00085.x.

Worsley, D., O. J. Aga, and A. Dalland, 1986, The geological history of Svalbard — Evolution of an Arctic archipelago.

Yenwongfai, H. D., N. H. Mondol, I. Lecomte, and J. I. Faleide, 2016, Prestack simultaneous inversion to predict lithology in the Realgrunnen Subgroup of the Goliat field, SW Barents Sea: 78th Annual International Conference and Exhibition, EAGE, Extended Abstracts, doi: 10.3997/2214-4609.201600964.

Zoeppritz, K., 1919, On the reflection and penetration of seismic waves through unstable layers: Erdbebenwellen VIIIB, Goettinger Nachrichten 1, 66–84.

Honore Dzekamelive Yenwongfai received a B.S. (hons) in geology and chemistry from the University of Buea, Cameroon, an M.S. in petroleum geology and petroleum geophysics from the University of Oslo, Norway (Quota Scheme Grant), and he is a Ph.D. candidate (grants from Research Council of Norway and industry partners) in petroleum geophysics at the University of Oslo. He joined Statoil ASA (2011) as a reservoir geologist in petroleum technology, and he is a senior geologist in reservoir characterization and modeling. His main research interests include seismic petrophysics and modeling in facies analysis.

Nazmul Haque Mondol received a B.S. in geology from the University of Dhaka, Bangladesh, an M.S. in geology and petroleum geosciences from the University of Dhaka, Bangladesh, and NTNU, Norway, respectively, and a Ph.D. in experimental rock physics from the University of Oslo, Norway. He is an associate professor at the University of Oslo and an advisor (adjunct position) at Norwegian Geotechnical Institute (NGI), Oslo, Norway. He was a postdoctoral fellow at the University of Oslo, Norway (grants from Research Council of Norway under the PETROMAKS program), before joining permanently as an associate professor at the University of Oslo. His research interests include rock physics, petrophysics, geomechanics, geophysics, and seismic to characterize source, reservoir, cap, and overburden rocks for exploration and exploitation of conventional and unconventional hydrocarbons and geologic storage of CO_2.

Jan Inge Faleide is a professor at the Department of Geosciences, University of Oslo, where he also received his cand. real. (1981) and dr. scient. (1990) degrees. He has been a project leader/PI for several interdisciplinary and international research projects focussing on the formation and evolution of sedimentary basins and continental margins. Most studies have been located offshore Norway and carried out in close collaboration with the petroleum industry. In these, geophysical and geologic data have been integrated at various scales, and many studies involved numerical and analog modeling. He received the StatoilHydros Research Award in 2009. He is affiliated with two research centers (CEED — Centre for Earth Evolution and Dynamics and ARCEx — Research Centre for Arctic Petroleum Exploration). He is a member of the Norwegian Academy of Science and Letters (DNVA), the Norwegian Academy of Technological Sciences (NTVA), and the Norwegian Scientific Academy for Polar Research.

Isabelle Lecomte received an M.S. (1987), a civ. eng. (1988), and a Ph.D. (1990; IFREMER grant) in geophysics from the University of Strasbourg, France. She was a postdoctoral fellow at NORSAR, Norway (grants from EU, 1991; Research Council of Norway, 1992), before joining permanently as a principal research geophysicist in R&D seismic modeling (1993–2016). She moved to the University of Bergen (2016 to present) as an associate professor in reservoir geophysics. She is also an adjunct associate professor at the University of Oslo (2012 to present) and a visiting associate professor at NORSAR (2016 to present). She received the 2001 EAGE Loránd Eötvös award and the 2014 Norwegian Geophysical award. Her main research interests include seismic modeling and imaging, with applications to seismic reflection, refraction, tomography, resolution analyses, and simulation of PSDM.

A biography and photograph of the author are not available.

4
5

Queries

1. Please check and confirm whether the mathematical term "⟩_b" used for "bulk density" is correct.

2. Table part labels are not allowed as per SEG style. Hence Tables 1a, 1b, 2a and 2b have been changed to Tables 1, 2, 3 and 4. Please check and confirm.

3. Please check the clarity of the term "between 1900 ms" in the sentence "For the simultaneous inversion (Figure 12a),....."

4. Please provide the publisher name for Worsley et al. (1986)".

5. Is it correct that author Leutscher does not wish to add an optional biography and photograph to this paper?

Funding Information

The following agencies have been identified as providing funding for your article. Please review the information carefully. If any changes are required, please submit those along with your other corrections to this article.

- Research Council of Norway (RCN)